Journal of Materials Chemistry A

ROYAL SOCIETY OF CHEMISTRY

PAPER

View Article Online
View Journal | View Issue

Cite this: J. Mater. Chem. A, 2022, 10, 24620

Bandgap engineering of covalent organic frameworks for boosting photocatalytic hydrogen evolution from water†

Yuxiang Chen,‡[a] Xiao Luo,‡[b] Jiejie Zhang,[a] Lu Hu,[a] Ting Xu,[a] Wei Li,[a] Lei Chen,[a] Mao Shen,[a] Shi-Bin Ren,*[a] De-Man Han,*[a] Guo-Hong Ning*[b] and Dan Li[b]

Received 15th September 2022
Accepted 2nd November 2022

DOI: 10.1039/d2ta07271h

rsc.li/materials-a

Solar light-promoted hydrogen production from water using covalent organic frameworks (COFs) as a photocatalyst is an attractive technique for clean energy sources. To boost the photocatalytic performance of COFs, it is necessary to narrow their bandgap. However, the bandgap engineering of COFs at the molecular level is less explored. Here, we synthesized four COFs using 2,4,6-tris(4-aminophenyl)-1,3,5-triazine with 1,3,5-triformylbenzene, 2,4,6-triformylphloroglucinol, 2,4,6-triformylphenol, and 2,4,6-triformylresorcinol, respectively, denoted as **COF-OH-*n*** (*n* = 0–3, representing the number of –OH groups). The different degrees of proton tautomerism in **COF-OH-*n*** arise from the different numbers of β-ketoenamine linkages in their skeletons, leading to the regulation of the visible light absorbing ability, bandgap, and band edge positions of **COF-OH-*n***. Due to irreversible proton tautomerism in **COF-OH-3**, it exhibited the most suitable band structures with a bandgap of 2.28 eV and a flat band of −0.62 eV among **COF-OH-*n***, resulting in the highest photocatalytic hydrogen production rate from water (*i.e.*, 9.89 mmol g^{-1} h^{-1}), while the other COFs delivered significantly low photocatalytic performances (*e.g.*, ∼0, 0.11, and 2.91 mmol g^{-1} h^{-1} for **COF-OH-1**, **COF-OH-0** and **COF-OH-2**, respectively).

Introduction

Photocatalytic production of hydrogen has been attracting great attention in view of efficient solar-to-chemical conversion,[1–4] since solar energy is the most attractive renewable replacement for fossil fuels because it is plentiful, inexhaustible, and widely distributed. In the past few decades, tremendous efforts have been made to explore various inorganic semiconductor photocatalysts,[5–8] since TiO_2 was first used as the photocatalyst for the water-splitting reaction by Honda and Fujishima.[9] However, most of the photocatalysts developed so far still exhibit unsatisfactory performances, mainly due to the poor absorbance of solar light, high recombination rate of photoinduced charge carriers, mismatch of the band position, and insufficient reactive sites on the photocatalyst surface.[10–12]

Covalent organic frameworks (COFs), a novel class of crystalline porous organic materials,[13–15] have been recently developed as promising photocatalysts because of their flexible structural and functional tunabilities. The designability of skeletons and the tunability of band structures in COFs are two key factors to be considered in developing highly efficient photocatalysts for water splitting.[16–19] Recently, an effective approach to tune the bandgaps by proton tautomerization in salicylideneaniline-based COFs (SA-COFs) has been developed.[20–23] The introduction of hydroxyl groups into SA-COFs leads to their reversible proton tautomerism, which could be triggered by water adsorption (SA-COF–H_2O) and desorption. In addition, the existence of the *trans*-keto forms in SA-COF–H_2O resulted in a redshift of the electronic adsorption in comparison with SA-COF, suggesting the narrower bandgap of SA-COF–H_2O than that of SA-COF.[20] Moreover, the modulation of the number of the β-ketoenamine linkages by increasing the number of hydroxyl groups in the precursors in SA-COFs could enhance the rigidity of the frameworks with appropriate bandgap, which brings about the superior photocatalytic performance of SA-COFs.[24] On the other hand, previous reports have shown that triazine knots with electron-deficient character could stabilize the negative charges on the COF and facilitate electron transfer.[25] It is envisioned that, by incorporating a 1,3,5-triazine core and β-ketoenamine linkages in SA-COFs, the thus-formed COFs with different energy band structures could be expected to exhibit high efficiency photocatalytic

[a]*Department of Chemistry, School of Pharmaceutical and Chemical Engineering, Taizhou University, 1139 Shifu Avenue, Taizhou 318000, Zhejiang Province, PR China. E-mail: renshibin@126.com; hdm@tzc.edu.cn*

[b]*College of Chemistry and Materials Science, Jinan University, Guangzhou, Guangdong 510632, PR China. E-mail: guohongning@jnu.edu.cn*

† Electronic supplementary information (ESI) available. See DOI: https://doi.org/10.1039/d2ta07271h

‡ These authors contributed equally to this work.

activity under a wide range of visible light irradiation wavelengths.[22]

Herein, we synthesized four different COFs based on 2,4,6-tris(4-aminophenyl)-1,3,5-triazine possessing a 1,3,5-triazine core with modified 1,3,5-triformylbenzene possessing different numbers of hydroxyl groups to form β-ketoenamine linkages in COFs (1,3,5-triformylbenzene, 2,4,6-triformylphloroglucinol, 2,4,6-triformylphenol, and 2,4,6-triformylresorcinol, corresponding to **COF-OH-*n*** (n = 0–3, representing the number of –OH groups)) (Scheme 1b). It is worth noting that varying the numbers of β-ketoenamine linkages in COFs could tune the reversibility between keto forms and enol forms in SA-COFs, leading to the regulation of the COF band structures (Scheme 1). In particular, **COF-OH-3** with suitable bandgaps and flat bands of 2.28 and −0.62 eV, respectively, exhibits the highest photocatalytic efficiency for visible light-driven hydrogen production from water (*i.e.*, 9.89 mmol g^{-1} h^{-1}) among these four synthesized COFs.

Results and discussion

Synthesis and characterization

2,4,6-Tris(4-aminophenyl)-1,3,5-triazine with equal moles of trialdehyde linkers bearing hydroxyl groups, namely, 1,3,5-triformylbenzene, 2,4,6-triformylphloroglucinol, 2,4,6-triformylphenol, or 2,4,6-triformylresorcinol, was dispersed in a mixture of dioxane and acetic acid (6 M) (10/1, v/v) under solvothermal conditions, giving yellow or red crystalline powders in high yields (82.1–91.3%), denoted as **COF-OH-*n***, where n = 0 to 3, respectively (Scheme 1). It should be noted that **COF-OH-1** and **COF-OH-2** have been newly prepared, while **COF-OH-0** and **COF-OH-3** have been previously synthesized.[26,27]

The crystalline structures of these COFs were determined by powder X-ray diffraction (PXRD) analysis. The experimental data of **COF-OH-0** and **COF-OH-3** well agreed with the reported literature,[26,27] indicating that the similar eclipsed stacking structure was obtained (Fig. S1, S4, and S5, and Table S1†). As

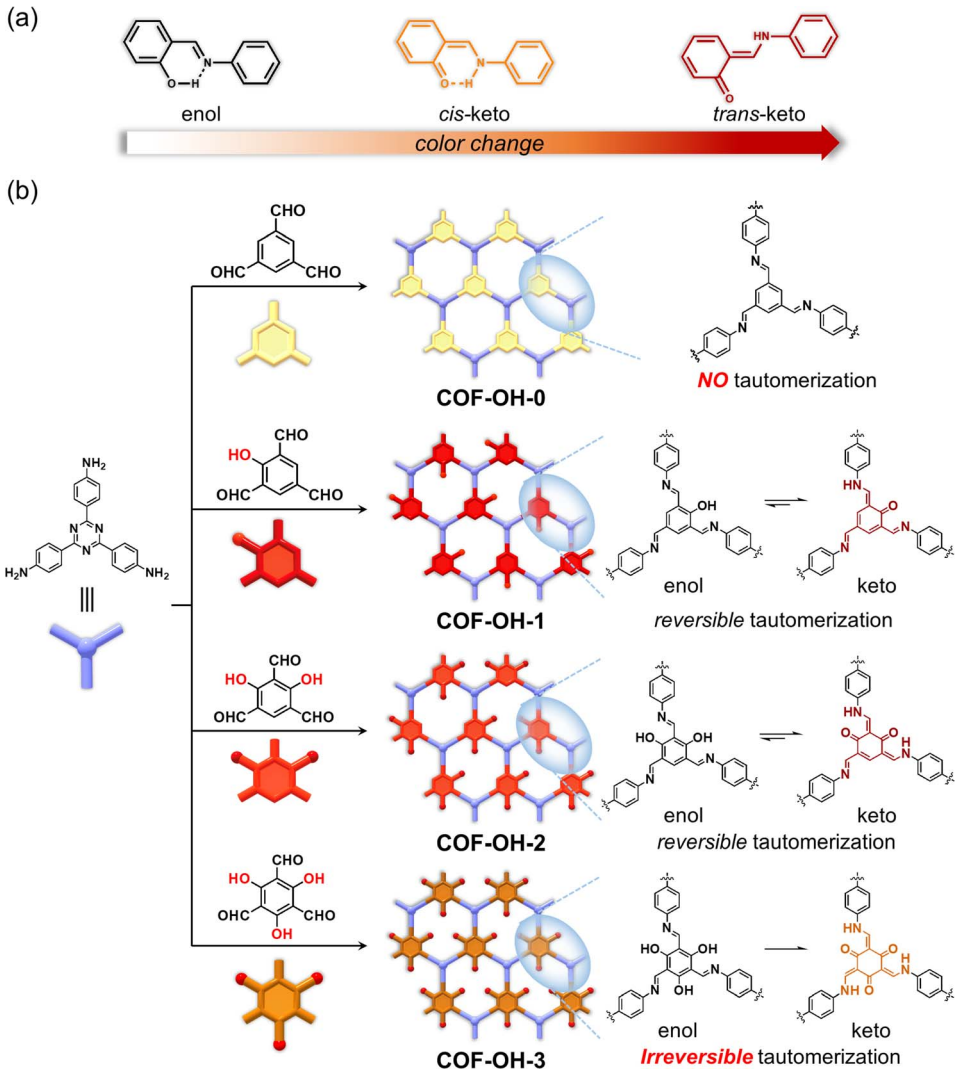

Scheme 1 (a) Proton tautomerism of salicylideneanilines inducing the color change; (b) schematic synthesis and structures of COF-OH-0, COF-OH-1, COF-OH-2, and COF-OH-3.

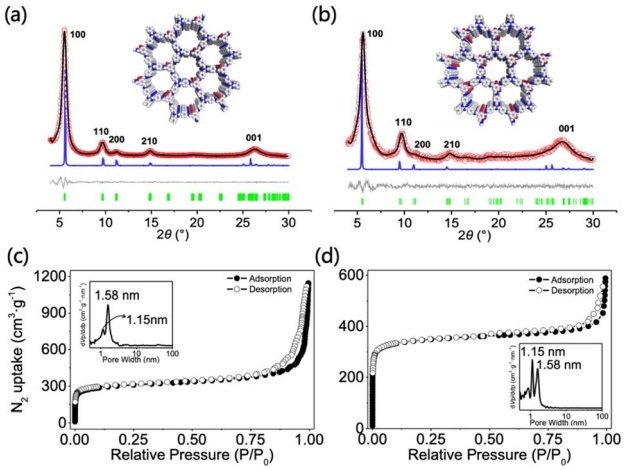

Fig. 1 PXRD characterization (experimental PXRD profile: red, refined profile: black, Bragg positions: green, difference: gray, and simulation patterns based on the AA stacking manner: blue) and top view simulated crystal structure shown in a spacing filling model (O: red; N: blue; C: white; hydrogen were omitted for clarity) for COF-OH-1 (a) and COF-OH-2 (b), respectively; N_2 adsorption (filled symbols) and desorption (open symbols) isotherms with the pore size distribution (inset) for COF-OH-1 (c) and COF-OH-2 (d), respectively.

shown in Fig. 1a, there are five obvious diffraction peaks in **COF-OH-1** PXRD patterns at $2\theta = 5.54°$, 9.70°, 11.16°, 14.92°, and 26.28°, respectively. Moreover, an eclipsed AA-stacking of **COF-OH-1** has been built (Fig. S5b†), and the simulated PXRD profile deduced from the structural model is well matched with the experimental curve of **COF-OH-1** (Fig. 1a). Furthermore, the Pawley refinement of the experimental PXRD data of **COF-OH-1** provided the unit cell parameters of $a = 3.41$ Å, $b = c = 18.71$ Å and the space group of $P\bar{1}$, with the agreement factors of $R_p = 5.11\%$ and $R_{wp} = 4.04\%$. As a result, the above-mentioned five diffraction peaks for **COF-OH-1** are assigned to (100), (110), (200), (210), and (001) reflections, respectively. In addition, the AB-stacking crystal model of **COF-OH-1** has also been constructed, and the PXRD simulations however do not match the experimental results (Fig. S2†). This is also true for **COF-OH-2** with the PXRD patterns at $2\theta = 5.58°$, 9.74°, 11.24°, 14.74°, 26.60° and the agreement factors of $R_p = 5.03\%$ and $R_{wp} = 3.99\%$ (Fig. 1b and S3, and Table S3†

To evaluate the porosity, nitrogen adsorption analyses of these four COFs were performed at 77 K. The Brunauer–Emmett–Teller (BET) surface areas of **COF-OH-0**, **COF-OH-1**, **COF-OH-2**, and **COF-OH-3** were found to be 1053, 1103, 1317, and 1003 $m^2 g^{-1}$ with the total pore volumes of 0.52, 1.36, 0.76, and 0.90 $cm^3 g^{-1}$, respectively (Fig. 1c, d, and S6†), revealing the high surface area and good porosity of the frameworks matching with the corresponding crystal structures. The pore size distribution of these COFs was also studied. As shown in Fig. 1c, d and S6†, **COF-OH-0** exhibited one main distribution centered at 1.65 nm, while dual-pore structures were observed in **COF-OH-1** (1.15 and 1.58 nm), **COF-OH-2** (1.15 and 1.58 nm), and **COF-OH-3** (1.01 and 1.58 nm), respectively.

These obtained COFs displayed good chemical stability and preserved their crystallinity upon 3 days of exposure to acids/bases and various solvents including 2 M HCl (aq.), 2 M TFA, 0.5 M NaOH (aq.), DBU, H_2O, DMF, dioxane, acetone, toluene, CH_3CN, $CHCl_3$, and MeOH (Fig. S7†). In addition, the thermogravimetric analysis (TGA) of **COF-OH-*n*** was also carried out, and they both exhibited high thermal stabilities with no significant weight loss between 80 and 550 °C under nitrogen (Fig. S8†).

The Fourier-transform infrared (FT-IR) spectra of as-synthesized COFs with their corresponding precursors were recorded. The disappearance of the N–H stretching band at ~3400 cm^{-1} corresponding to the $-NH_2$ groups and the absence of aromatic aldehyde Ar–CHO characteristic absorption bands at 1715–1695 cm^{-1} clearly indicate the formation of the imine bond (Fig. S9†). To further confirm the structures of these COFs, the ^{13}C cross-polarization/magic-angle spinning (CP-MAS) solid-state NMR experiments were also conducted. It should be noted that the NMR data of the reported COFs **COF-OH-0** and **COF-OH-3** are consistent with the reported literature.[27,28] As shown in Fig. S10b†, the peak at 157.2 ppm can be identified, which is assigned to carbon in imine –CN resonance in **COF-OH-1**. In addition, the weak peaks at 140.0 and 183.2 ppm assigned to the enamine carbon (CC*–N) and the carbonyl carbon (*CO), respectively, could also be found, suggesting the existence of the keto form as a minor component in **COF-OH-1**.[20] For **COF-OH-2** (Fig. S10c†), the resonance signals at 140.0 and 183.0 ppm could be found as two strong peaks, which were also assigned to carbon in CC*–N and *CO groups, indicating that the keto form is the major component in **COF-OH-2**. This is also similar for **COF-OH-3** (Fig. S10d†). Furthermore, the peaks at 169.0–169.6 ppm could be observed in all the COFs, which should be assigned to carbon resonance signals from the triazine core in

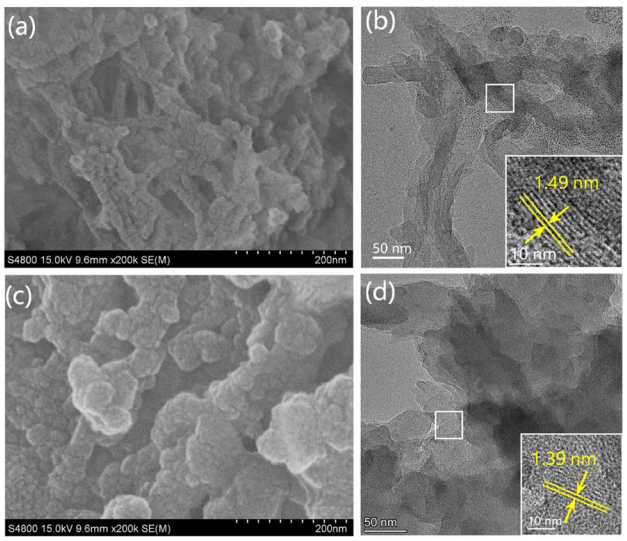

Fig. 2 SEM images of COF-OH-1 (a) and COF-OH-2 (c), respectively; HRTEM images with enlarged selected areas from the white box showing the corresponding lattice fringes of COF-OH-1 (b) and COF-OH-2 (d), respectively.

COF-OH-0–3 (Fig. S10†), indicating the successful synthesis of the four COFs.

The surface morphologies and the microstructures of the COFs were investigated by scanning electron microscopy (SEM) and high-resolution transmission electron microscopy (HRTEM). As exhibited in Fig. S11,† **COF-OH-0**, **COF-OH-2**, and **COF-OH-3** displayed similarly irregular block-shaped appearance. **COF-OH-1** displayed much smaller flaky aggregates than the others (Fig. S11c†). HRTEM images exhibit long-range ordered microstructures of the four COFs. As shown in Fig. 2 and S12,† the lattice fringes of COFs were clearly visualized, suggesting the high crystallinity of this sample. In addition, the light–dark lattice fringes in the HRTEM image were measured to be 1.4, 1.5, and 1.4 nm for **COF-OH-0**, **COF-OH-1**, and **COF-OH-2**, corresponding to their (100) diffractions, respectively, while the distance between two adjacent lattice faces of 0.45 nm attributed to the (310) diffraction was found for **COF-OH-3** (Fig. S12†).

Optical properties

The UV-vis diffuse reflectance spectra of **COFs** were recorded to understand the visible light-harvesting abilities, which are important for photocatalytic hydrogen evolution from water. Due to the incapability of proton tautomerization for **COF-OH-0**, the COF shows the narrowest absorption spectrum ranging from 300 to 480 nm. In sharp contrast, **COF-OH-1**, **COF-OH-2**, and **COF-OH-3** exhibited much broader visible light absorbance in the range of 300–680 nm. Interestingly, **COF-OH-1** displayed the broadest absorption band, attributed to the formation of the *trans*-keto form, leading to a deep red color that should enhance the visible light-harvesting abilities.[20,21] With two hydroxyl groups, **COF-OH-2** also featured reversible keto–enol tautomerization and the push–pull effect, resulting in strong visible light absorption.[22,24] Due to the irreversible keto–enol tautomerization in **COF-OH-3**, it only features pull effect and exhibits moderate visible light absorption.[27,29] In addition, the optical bandgaps of **COF-OH-*n*** (n = 0–3) by using the Tauc plot according to the data from UV-vis diffuse reflectance spectra were calculated to be 2.68, 1.90, 2.02, and 2.28 eV (Fig. S13†) and all of them were narrower than 3.1 eV, implying that they are promising photocatalysts for efficient water-splitting reaction.[12] To evaluate charge generation efficiency of COFs under light irradiation, the photocurrent measurements were performed. Interestingly, the photocurrent of **COF-OH-3** shows an instant increase (0 to 0.8 nA cm^{-2}) and then a quick decrease followed by an equilibrium (~0.3 nA cm^{-2}) when the light is on, which may be due to the quick charge recombination in **COF-OH-3** and the established equilibrium between the electrolyte solution and ITO electrode coated with the **COF-OH-3** layer upon irradiation.[30–32] Nevertheless, **COF-OH-3** delivered remarkably higher efficient charge generation upon visible light irradiation than that of other COFs (Fig. 3b). These results clearly demonstrated that the introduction of different numbers of –OH groups indeed modulated the keto–enol tautomerization, leading to tuning the visible light-harvesting abilities and charge generation efficiency of the COFs.

To estimate the flat-band potentials (FBPs) of the COFs, Mott–Schottky analysis was performed in 0.1 M Na_2SO_4 solution. All the COFs exhibited positive slopes in the Mott–Schottky plots, suggesting the n-type semiconductor nature of these COFs (Fig. S14†). In addition, their corresponding FBPs were calculated *vs.* the standard hydrogen electrode (SHE) as −0.51, −0.24, −0.55, and −0.62 V (Fig. 3c and Table S3†), respectively. Generally, the bottom of the conduction band (CB) or LUMO stays very close to the FBP in n-type semiconductors and the HOMO level could be calculated considering the optical bandgap.[33,34] As a result, the band position and bandgap of COFs *vs.* SHE along with the potential of H^+/H_2 and $HA^{\bullet}/H_2A$ are displayed in Fig. 3c.[35] The LUMO energy level of COFs is more negative with 0.36 0.09, 0.40, and 0.47 V than H^+/H_2 potential (−0.15 V), respectively. Considering the visible light absorption ability, charge generation efficiency and LUMO energy levels of the as-prepared COFs, all the COFs might be suitable photocatalysts for water splitting in 0.1 M ascorbic acid aqueous solution, but **COF-OH-3** is expected to be the most promising one.

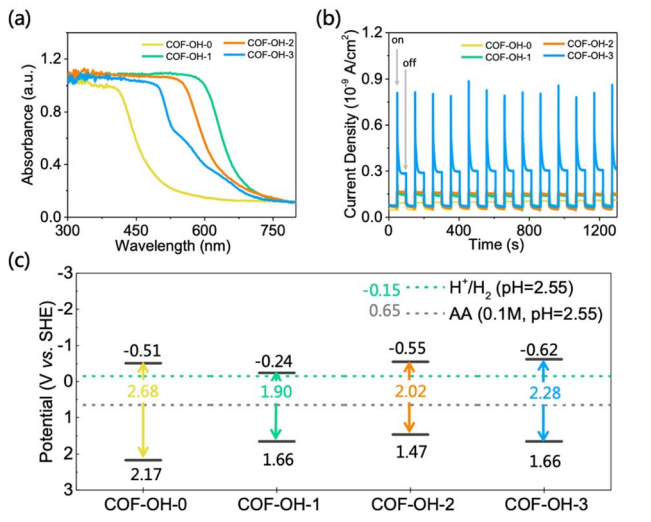

Fig. 3 UV-vis diffuse reflectance spectra of COF-OH-0–3 (a); photocurrent–time curves under $\lambda \geq 420$ nm light irradiation of COF-OH-0–3 (b); band position and bandgap of COFs *vs.* the standard hydrogen electrode (SHE) along with the potential of H^+/H_2 and one-hole ($HA^{\bullet}/H_2A$) oxidation of L-ascorbic acid under current conditions (c).

Photocatalytic performance

Encouraged by the above characterization results, photocatalytic hydrogen evolution from water experiments have been conducted using visible light ($\lambda \geq 420$ nm, 300 W xenon lamp). Ascorbic acid (AA) as a sacrificial agent was chosen and the content of Pt as a co-catalyst was optimized to be 1 wt% (Fig. S15 and S16†). Under these optimized reaction conditions, the photocatalytic performance of the COFs has been investigated. The hydrogen evolution rates were determined to be 0.11 mmol g^{-1} h^{-1} for **COF-OH-0**, 2.91 mmol g^{-1} h^{-1} for **COF-OH-2**, and 9.89 mmol g^{-1} h^{-1} for **COF-OH-3** (Fig. 4b). It should be noted

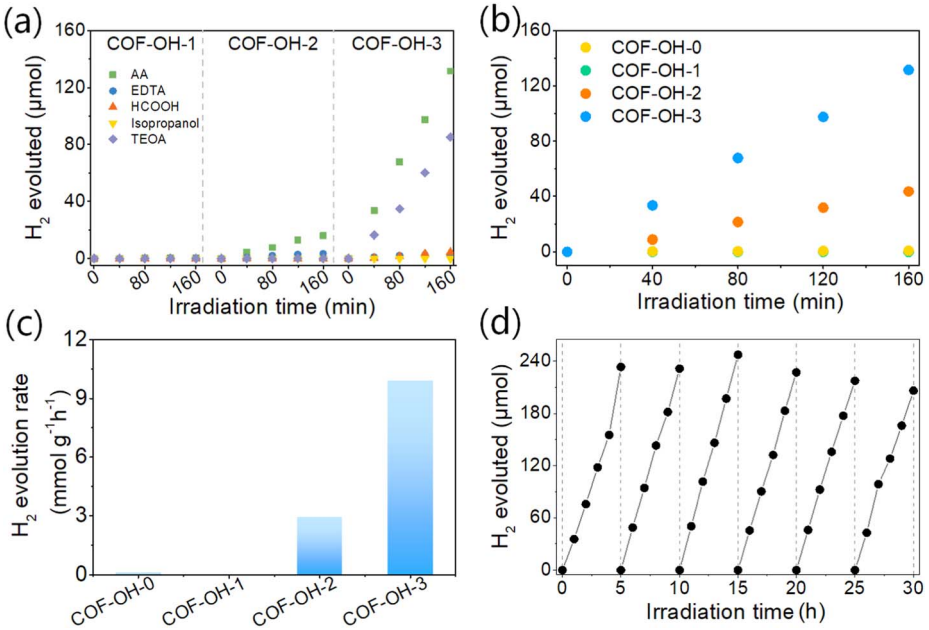

Fig. 4 Hydrogen evolution for **COF-OH-0–3** using different sacrificial agents under visible light ($\lambda \geq 420$ nm) (a); time course for photocatalytic H_2 production under visible light ($\lambda \geq 420$ nm) of **COF-OH-0–3** (5 mg of catalyst with 1 wt% Pt in 25 mL 0.1 M ascorbic acid aqueous solution) (b); comparison of photocatalytic hydrogen evolution rates (c); plot of sacrificial photocatalytic hydrogen evolution *versus* time for **COF-OH-3** under solar simulator irradiation. The sample was degassed every 5 h to prevent saturation of the detector, and after 15 h, 1 mmol of ascorbic acid was added (d).

that the weakest visible light-harvesting ability of **COF-OH-0** should be the reason for its relatively poor photocatalytic performance. Nevertheless, **COF-OH-2** and **COF-OH-3** exhibit superior photocatalytic properties, which may arise from their good hydrophilicity and suitable energy level for hydrogen evolution from water.[36–38] The apparent quantum yield (AQY) for **COF-OH-3** was found to be 0.15% (50 mg sample, $\lambda = 420$ nm, Fig. S17†). Moreover, although **COF-OH-1** exhibited strongest visible light absorption ability, there was no hydrogen detected (Fig. 4a and b) under the same experiment conditions, which may be due to the minimal driving force for proton reduction of **COF-OH-1** as revealed by the Mott–Schottky analysis (Fig. 3e). To further investigate the photocatalytic stability and recyclability of the COFs, **COF-OH-3** was chosen as the representative, since it exhibits the highest photocatalytic water splitting performance among the four COFs. The hydrogen evolution experiments of **COF-OH-3** were conducted for 30 h irradiation time (Fig. 4c). No significant loss of the photoactivity was observed over the period of time, and even after recycling six times, both PXRD and FT-IR spectra were comparable to those of the fresh prepared sample of **COF-OH-3** (Fig. S18 and S19†), revealing the good photocatalytic stability and recyclability of **COF-OH-3**.

Conclusions

In summary, four COFs, namely, **COF-OH-*n*** (n = 0–3) bearing the triazine core and a number of –OH groups have been synthesized and comprehensively characterized. Interestingly, the introduction of different numbers of –OH groups can effectively control proton tautomerism in **COF-OH-*n***, leading to the regulation of their visible light absorbing ability, bandgap, and band edge positions, which are key factors for photocatalytic water-splitting reactions. Specifically, **COF-OH-3** exhibited irreversible proton tautomerism and featured the most suitable band structures with a bandgap of 2.28 eV and a flat band of −0.62 eV among **COF-OH-*n***. Therefore, it delivered the highest photocatalytic hydrogen production rate of 9.89 mmol g^{-1} h^{-1} from water, which is remarkably higher than those of other COFs (*e.g.*, ~0, 0.11 and 2.91 mmol g^{-1} h^{-1} for **COF-OH-1**, **COF-OH-0** and **COF-OH-2**, respectively). Our investigation paves a new way for designing advanced porous materials with high photocatalytic activities for hydrogen production from water.

Experimental section

Materials

The compounds 1,3,5-tris-(4-aminophenyl)triazine,[39] 2-hydroxy-1,3,5-benzenetricarboxaldehyde,[40] and 2,4-dihydroxy-1,3,5-benzenetricarboxaldehyde[41] were prepared according to literature procedures. All other reagents and solvents were purchased from commercial suppliers and used as received.

Instruments and measurements

Powder X-ray diffraction (PXRD) analyses were carried out by using an X-ray diffractometer (D8 Advance) using Cu-Kα radiation ($\lambda = 1.54056$ Å) at room temperature. Solid-state ^{13}C spectra were recorded on a Bruker AVANCE III HD 600 MHz

spectrometer. Solid-state UV-vis spectra were recorded on a Hitachi U-4100 spectrophotometer with $BaSO_4$ as the reference. Fourier-transform infrared spectroscopy (FTIR) spectra were recorded with KBr pellets using a Thermo Scientific Nicolet iS10. Nitrogen adsorption and desorption isotherms were measured at 77 K using a Micromeritics ASAP 2020 system. The samples were degassed at 100 °C for 10 h before the measurements. The surface areas were calculated from the adsorption data using the Brunauer–Emmett–Teller (BET) equation. Field-emission scanning electron microscopy (SEM) was performed on a Hitachi S-4800. The thermogravimetric analysis (TGA) was performed on a Mettler Toledo TGA2 instrument over the temperature range of 25 to 800 °C under a nitrogen atmosphere with a heating rate of 10 °C min^{-1}.

Electrochemical measurement

The Mott–Schottky plots were obtained at 1.0, 2.0, and 3.0 kHz frequencies on a CHI760E electrochemical workstation in a three-electrode cell. The counter electrode was a Pt wire, and the reference electrode was a saturated calomel electrode (SCE). For the preparation of the working electrodes, the as-synthesized samples (2 mg) were added into a mixed solution of Nafion (5 μL) and ethanol (100 μL), and then, the catalyst suspension (5 μL × 3) was dropped onto the ITO glass substrate, forming a film after drying. An aqueous solution containing 0.1 M Na_2SO_4 was used as the electrolyte.

Photocatalytic hydrogen production

Typically, 5 mg sample was dispersed in a 0.1 M ascorbic acid water solution (25 mL). Then, hexachloroplatinic acid (5 μL) as a Pt precursor was added. After that, the suspension solution was placed in a 160 mL optical reaction vessel (purchased from Perfect Light) with flowing tap water at 4 °C. Then, the suspension was stirred and purged for 20 min to remove air. The photocatalysis reaction was carried out using a 300 W Xe lamp (LX-300F) equipped with a UV cut off filter ($\lambda \geq 420$ nm) with stirring. The hydrogen was quantified using an online gas chromatograph (GC-2014C, TCD detector, nitrogen as a carrier gas) with a calibration plot of the hydrogen standard curve.

Apparent quantum yield (AQY)

The AQY for **COF-OH-3** was determined at $\lambda = 420$ nm (300 W Xe lamp equipped with a band-pass filter $\lambda = 420$ nm). In addition, the AQY was calculated using the following equation:[42–44]

$$\mathrm{AQY}\ (\%) = \frac{2 \times \text{number of evolved } H_2 \text{ molecules}}{\text{number of incident photons}} \times 100\% = \frac{2 \times v \times N_A}{p \times S \times \lambda/hc} \times 100\%$$

where v is the H_2 production rate (mol s^{-1}), N_A is the Avogadro constant (6.02×10^{23} mol^{-1}), h is the Planck constant (6.63×10^{-34} J s^{-1}), c is vacuum light velocity (3×10^8 m s^{-1}), p is the average intensity of irradiation which was determined to be 342 W m^{-2}, and S is the irradiation area ($S = 1.81 \times 10^{-3}$ m^2).

Stability tests of COF-OH-3 for photocatalytic hydrogen production

Six runs of consecutive photocatalytic hydrogen production were carried out to evaluate the cyclability and stability of **COF-OH-3** (5 hours each run). After each cycle, the reaction system was degassed. In addition, after 15 h, 176 mg ascorbic acid was added to the reaction system.

Synthesis of COF-OH-0. 1,3,5-Benzenetricarboxaldehyde (48.6 mg, 0.3 mmol) and 2,4,6-tris(4-aminophenyl)-1,3,5-triazine (106.3 mg, 0.3 mmol) were placed into a 25 mL thick wall Schlenk tube and dissolved in 6.0 mL of the dioxane by sonicating for 10 min. Then, acetic acid (6 M, 0.6 mL) was added, and the tube was flash-frozen in a liquid nitrogen bath and degassed by three freeze–pump–thaw cycles. The tube was sealed and then heated at 120 °C for 3 days. After being cooled to room temperature, the precipitate was filtered and washed with *N*,*N*-dimethylformamide, dioxane, methanol, and tetrahydrofuran, respectively. After that, the product was further purified by Soxhlet extraction using tetrahydrofuran. After being dried at 60 °C with reduced pressure, the product was obtained as a light-yellow powder (126.6 mg) in 91.3% isolated yield.

Synthesis of COF-OH-1. By employing the above-mentioned procedure for preparing **COF-OH-0** using 2-hydroxybenzene-1,3,5-tricarbaldehyde (53.4 mg, 0.3 mmol) instead of 1,3,5-benzenetricarboxaldehyde as starting material, a dark red powder (125.1 mg) of **COF-OH-1** with 87.2% isolated yield was obtained.

Synthesis of COF-OH-2. By employing the above-mentioned procedure for preparing **COF-OH-0** using 2,4-dihydroxybenzene-1,3,5-tricarbaldehyde (58.2 mg, 0.3 mmol) instead of 1,3,5-benzenetricarboxaldehyde as starting material, an orange powder (121.8 mg) of **COF-OH-2** with 82.1% isolated yield was obtained.

Synthesis of COF-OH-3. By employing the above-mentioned procedure for preparing **COF-OH-0** using 2,4,6-trihydroxybenzene-1,3,5-tricarbaldehyde (63.0 mg, 0.3 mmol) instead of 1,3,5-benzenetricarboxaldehyde as starting material, a yellow powder (129.4 mg) **COF-OH-3** with 84.5% isolated yield was obtained.

Author contributions

Y. Chen, X. Luo, J. Zhang, L. Hu, and T. Xu performed the experiments, data analysis and wrote the original draft, and revised it. S.-B. Ren, D.-M. Han, G.-H. Ning, and D. Li supervised the whole project. W. Li, L. Chen, and M. Shen helped with data acquisition and analysis. All authors discussed the results and commented on the manuscript.

Conflicts of interest

There are no conflicts to declare.

Acknowledgements

Financial support from the Natural Science Foundation of China (grant no. 21471110 and 21575097), the Zhejiang

Provincial Natural Science Foundation of China (grant no. LY22E030008, LY19E030001, LGF19B050002, and LQ20B010004), the Training Fund Project of Taizhou University (Special Fund for Higher Education Research, grant no. 2019PY030), supported through the Basic Public Welfare Research Project of Zhejiang Province under grant no. LGC19B050006, and the University of Taizhou is gratefully acknowledged. G.-H. Ning is grateful for the financial support from the Guangdong Basic and Applied Basic Research Foundation (nos. 2019B151502024 and 2021A0505030037) and Guangdong Province Pearl River Scholar Funded Scheme (2019). National Natural Science Foundation of China (nos. 21975104 and 22150004), the Guangdong Major Project of Basic and Applied Research (no. 2019B030302009) also supported this work financially.

References

1 Q. Wang and K. Domen, *Chem. Rev.*, 2020, **120**, 919–985.
2 M. G. Walter, E. L. Warren, J. R. McKone, S. W. Boettcher, Q. Mi, E. A. Santori and N. S. Lewis, *Chem. Rev.*, 2010, **110**, 6446–6473.
3 X. Tao, Y. Zhao, S. Wang, C. Li and R. Li, *Chem. Soc. Rev.*, 2022, **51**, 3561–3608.
4 B. Samanta, A. Morales-Garcia, F. Illas, N. Goga, J. A. Anta, S. Calero, A. Bieberle-Hutter, F. Libisch, A. B. Munoz-Garcia, M. Pavone and M. Caspary Toroker, *Chem. Soc. Rev.*, 2022, **51**, 3794–3818.
5 Z. Zou, J. Ye, K. Sayama and H. Arakawa, *Nature*, 2001, **414**, 625–627.
6 D. Friedmann, A. F. Lee, K. Wilson, R. Jalili and R. A. Caruso, *J. Mater. Chem. A*, 2019, **7**, 10858–10878.
7 S. Chen, D. Huang, P. Xu, W. Xue, L. Lei, M. Cheng, R. Wang, X. Liu and R. Deng, *J. Mater. Chem. A*, 2020, **8**, 2286–2322.
8 X. Han, S. Ding, H. Hu and S. Wang, *J. Mater. Chem. A*, 2022, **10**, 18509–18541.
9 A. Fujishima and K. Honda, *Nature*, 1972, **238**, 37–38.
10 M. Z. Rahman, M. G. Kibria and C. B. Mullins, *Chem. Soc. Rev.*, 2020, **49**, 1887–1931.
11 J. Ran, J. Zhang, J. Yu, M. Jaroniec and S. Z. Qiao, *Chem. Soc. Rev.*, 2014, **43**, 7787–7812.
12 Y. Wang, H. Suzuki, J. Xie, O. Tomita, D. J. Martin, M. Higashi, D. Kong, R. Abe and J. Tang, *Chem. Rev.*, 2018, **118**, 5201–5241.
13 A. P. Cote, A. I. Benin, N. W. Ockwig, M. O'Keeffe, A. J. Matzger and O. M. Yaghi, *Science*, 2005, **310**, 1166–1170.
14 N. Huang, P. Wang and D. Jiang, *Nat. Rev. Mater.*, 2016, **1**, 16068.
15 C. S. Diercks and O. M. Yaghi, *Science*, 2017, **355**, 923.
16 H. V. Babu, M. G. M. Bai and M. Rajeswara Rao, *ACS Appl. Mater. Interfaces*, 2019, **11**, 11029–11060.
17 K. Geng, T. He, R. Liu, K. T. Tan, Z. Li, S. Tao, Y. Gong, Q. Jiang and D. Jiang, *Chem. Rev.*, 2020, **120**, 8814–8933.
18 H. Wang, H. Wang, Z. Wang, L. Tang, G. Zeng, P. Xu, M. Chen, T. Xiong, C. Zhou, X. Li, D. Huang, Y. Zhu, Z. Wang and J. Tang, *Chem. Soc. Rev.*, 2020, **49**, 4135–4165.
19 L. Stegbauer, K. Schwinghammer and B. V. Lotsch, *Chem. Sci.*, 2014, **5**, 2789–2793.
20 G.-H. Ning, Z. Chen, Q. Gao, W. Tang, Z. Chen, C. Liu, B. Tian, X. Li and K. P. Loh, *J. Am. Chem. Soc.*, 2017, **139**, 8897–8904.
21 X. Li, Q. Gao, J. Aneesh, H.-S. Xu, Z. Chen, W. Tang, C. Liu, X. Shi, K. V. Adarsh, Y. Lu and K. P. Loh, *Chem. Mater.*, 2018, **30**, 5743–5749.
22 N. Singh, D. Yadav, S. V. Mulay, J. Y. Kim, N.-J. Park and J.-O. Baeg, *ACS Appl. Mater. Interfaces*, 2021, **13**, 14122–14131.
23 J. Yang, A. Acharjya, M.-Y. Ye, J. Rabeah, S. Li, Z. Kochovski, S. Youk, J. Roeser, J. Grueneberg, C. Penschke, M. Schwarze, T. Wang, Y. Lu, R. van de Krol, M. Oschatz, R. Schomacker, P. Saalfrank and A. Thomas, *Angew. Chem., Int. Ed.*, 2021, **60**, 19797–19803.
24 H. Wang, C. Qian, J. Liu, Y. Zeng, D. Wang, W. Zhou, L. Gu, H. Wu, G. Liu and Y. Zhao, *J. Am. Chem. Soc.*, 2020, **142**, 4862–4871.
25 V. S. Vyas, F. Haase, L. Stegbauer, G. Savasci, F. Podjaski, C. Ochsenfeld and B. V. Lotsch, *Nat. Commun.*, 2015, **6**, 8508.
26 Q. Gao, L. Bai, X. Zhang, P. Wang, P. Li, Y. Zeng, R. Zou and Y. Zhao, *Chin. J. Chem.*, 2015, **33**, 90–94.
27 R. Gomes and A. Bhaumik, *RSC Adv.*, 2016, **6**, 28047–28054.
28 J. Dong, Y. Wang, G. Liu, Y. Cheng and D. Zhao, *CrystEngComm*, 2017, **19**, 4899–4904.
29 R. Wang, W. Kong, T. Zhou, C. Wang and J. Guo, *Chem. Commun.*, 2021, **57**, 331–334.
30 N. Iqbal, I. Khan, Z. H. Yamani and A. Qurashi, *Sci. Rep.*, 2016, **6**, 32319.
31 F.-M. Zhang, J.-L. Sheng, Z.-D. Yang, X.-J. Sun, H.-L. Tang, M. Lu, H. Dong, F.-C. Shen, J. Liu and Y.-Q. Lan, *Angew. Chem., Int. Ed.*, 2018, **57**, 12106–12110.
32 X. Wu, M. Zhang, Y. Xia, C. Ru, P. Chen, H. Zhao, L. Zhou, C. Gong, J. Wu and X. Pan, *J. Mater. Chem. A*, 2022, **10**, 17691–17698.
33 S. Ghosh, A. Nakada, M. A. Springer, T. Kawaguchi, K. Suzuki, H. Kaji, I. Baburin, A. Kuc, T. Heine, H. Suzuki, R. Abe and S. Seki, *J. Am. Chem. Soc.*, 2020, **142**, 9752–9762.
34 S. Bi, W. Zhang, J. Xu, D. Wu, F. Zhang, C. Yang, X. Wang, L. Liu, Y. Han and Q. Liang, *Nat. Commun.*, 2019, **10**, 2467.
35 X. Wang, L. Chen, S. Y. Chong, M. A. Little, Y. Wu, W.-H. Zhu, R. Clowes, Y. Yan, M. A. Zwijnenburg, R. S. Sprick and A. I. Cooper, *Nat. Chem.*, 2018, **10**, 1180–1189.
36 K. Takanabe, *ACS Catal.*, 2017, **7**, 8006–8022.
37 M. Z. Rahman, C. W. Kwong, K. Davey and S. Z. Qiao, *Energy Environ. Sci.*, 2016, **9**, 709–728.
38 T. Li, T. Hu, L. Dai and C. M. Li, *J. Mater. Chem. A*, 2020, **8**, 23674–23698.
39 R. Gomes, P. Bhanja and A. Bhaumik, *Chem. Commun.*, 2015, **51**, 10050–10053.
40 A. A. Anderson, T. Goetzen, S. A. Shackelford and S. Tsank, *Synth. Commun.*, 2000, **30**, 3227–3232.
41 S. Haldar, D. Chakraborty, B. Roy, G. Banappanavar, K. Rinku, D. Mullangi, P. Hazra, D. Kabra and

R. Vaidhyanathan, *J. Am. Chem. Soc.*, 2018, **140**, 13367–13374.
42 X. Zhang, B. Peng, S. Zhang and T. Peng, *ACS Sustainable Chem. Eng.*, 2015, **3**, 1501–1509.
43 M.-Y. Gao, C.-C. Li, H.-L. Tang, X.-J. Sun, H. Dong and F.-M. Zhang, *J. Mater. Chem. A*, 2019, **7**, 20193–20200.
44 C. Li, J. Liu, H. Li, K. Wu, J. Wang and Q. Yang, *Nat. Commun.*, 2022, **13**, 2357.